Journal of Materials Chemistry A

Accepted Manuscript

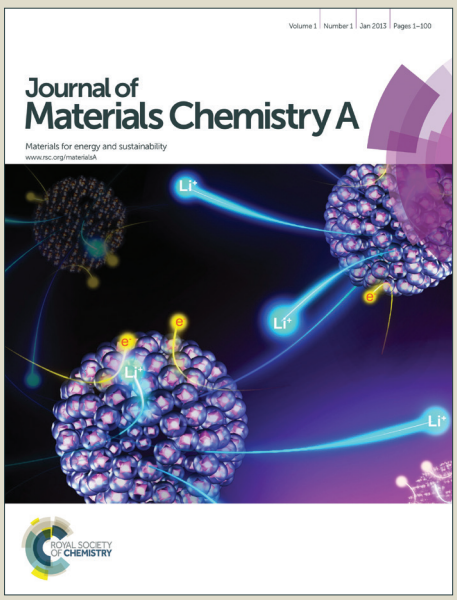

ROYAL SOCIETY OF CHEMISTRY

www.rsc.org/materialsA

Journal Name

ARTICLE

Investigation of hollow nitrogen-doped carbon spheres as non-precious Fe-N_4 based oxygen reduction catalyst

Received 00th January 20xx,
Accepted 00th January 20xx

DOI: 10.1039/x0xx00000x

www.rsc.org/

Jakkid Sanetuntikul[a], Chitiphon Chuaicham[b], Young-Woo Choi[c] and Sangaraju Shanmugam[a]*

The development of inexpensive non-precious oxygen reduction catalysts has become one of the most important efforts in polymer electrolyte membrane fuel cells. In this report, we synthesized a non-precious electrocatalyst from a single precursor, iron (III) diethyelene triaminepentaacetate, using a heat-treatment effect to prepare an active catalyst. A series of catalysts were prepared at different temperatures leading to different degrees of graphitization, heteroatom content and activity. In 0.1M KOH electrolyte solution, the oxygen reduction reaction (ORR) onset potential of the HNCS71 catalyst was as high as 0.97V, and half-wave potentials were only 20mV lower than for Pt/C. X-ray absorption measurements of Fe K-edge showed the structure of Fe-N_4 centers, formed in HNCS71, which were responsible for the ORR activity. An alkaline exchange membrane fuel cell made with HNCS71 as cathode was tested in H_2-O_2 single cell and showed a maximum power density of ~68 mW cm^{-2}. The 100-hour fuel cell durability test of HNCS71 cathode showed decays in current density of about 14% at 0.4 V. Therefore, the HNCS catalyst appears to be a promising new class of non-precious catalyst for fuel cell applications.

Introduction

Polymer electrolyte membrane fuel cells (PEMFCs) are considered to be one of the most promising power sources, utilizing hydrogen and air to generate electricity, providing high power density with efficient energy-conversion.[1] One of the most essential parts of the PEMFC is the catalyst. Platinum (Pt) is the best-known catalyst in fuel cell technology for the oxygen reduction reaction (ORR), however, Pt's low natural abundance and high cost are the key limitations to the commercialization of PEMFC. Additionally, the sluggish ORR of Pt-based catalysts during fuel cell operation is one of the most limiting factors of the energy-conversion efficiency of PEMFCs.[2,3] Thus, developing a cost-effective, efficient, and highly durable ORR catalyst has become one of the most important topics in the fuel cell community. Research efforts have been focused on the development of non-precious catalysts to replace Pt-based catalysts, and specifically, on producing novel non-precious catalysts with improved ORR activity.

While several new non-precious catalysts with improved catalytic activity and durability have emerged, currently their activity is lower than that of a Pt catalyst.[4–6] To modify the catalysts' electrical properties and chemical activity, which can improve ORR performance, substitution of a heteroatom with phosphorus (P), boron (B), sulphur (S), or nitrogen (N) into the carbon framework has generally been used. Gong *et al*[7] synthesized vertically aligned nitrogen-containing carbon nanotubes (VA-NCNTs) as an electrocatalyst, which showed enhanced ORR activity. The improved activity was attributed to the N atom doped on the C framework, which creates a positive charge on the C atom, which is in turn favourable for oxygen adsorption. Yang *et al*[8] synthesized sulphur-doped graphene, which resulted in excellent durability and ORR activity. Doping of a heteroatom on carbon can alter the electronic arrangement in a positive manner. However, heteroatom doped carbon materials still have lower performance than Pt-based catalysts. So, serious efforts to design and synthesize a catalyst with better activity and durability for practical application continue.[9,10]

Recent studies have confirmed that non-precious catalysts based on metal coordinated with nitrogen-doped carbon (M-N-C) are promising candidates for cathode electrocatalysts. In the last decade, many studies have achieved improvement in the activity, performance and stability of M-N-C catalysts, where M is usually either Fe or Co. Peng *et al*[11] synthesized Fe-N doped on high surface area graphene, which showed superior ORR onset, half-wave potential and excellent durability. Lefèvre *et al*[12] reported that novel Fe-N-C catalysts, with the metal ions coordinated with N atoms on the carbon lattice, can act as active sites for ORR. Based on the above research, M-N-C catalysts have the potential to replace the state-of-art Pt/C catalyst in practical fuel cell applications. To achieve such high performance the important factors for the catalyst are the metal, nitrogen, carbon and heat-treatment temperature. In particular, the heat-treatment temperature seems to be the most significant parameter for improving the activity and stability of the ORR of M-N-C based catalysts. In these methods, the synthesis of non-precious catalysts were carried out using several precursors and process is tedious. The novelty of our work is related to the synthesis

[a]Department of Energy Systems Engineering, Daegu Gyeongbuk Institute of Science and Technology (DGIST), Daegu, 711-873, Republic of Korea.
[b]Department of Chemistry, Faculty of Science, Mahidol University, Bangkok, 10400, Thailand
[c]Korea Institute of Energy Research (KIER), New and Renewable Energy village, 1110-6, Baek-ryunri, Haseomyun, Bu-angun, Jeonlabukdo, Republic of Korea.
E-mail:sangarajus@dgist.ac.kr ; Fax: (+82) 53 785 6409.
†Electronic Supplementary Information (ESI) available: additional RDE, XPS and XAS results. See DOI: 10.1039/c000000x/

of M-N-C catalyst using a single precursor, Iron (III) diethylene triaminepentaacetate, which acts as a source for metal, nitrogen and carbon. Further, more we systematically investigated the effects of heat-treatment via direct pyrolysis under the autogenic pressure without using any inert gas by Swagelok union cell on the oxygen reduction reaction. Catalyst characterization results such as X-ray absorption spectroscopy (XAS) has been employed to clarify markedly ORR electrochemical active site and the composition of HNCSs are included in this report.

Experimental

Synthesis of hollow nitrogen-doped carbon spheres (HNCSs)

Hollow nitrogen doped carbon spheres (HNCSs) were prepared according to previously reported procedures.[13] Briefly, HNCSs synthesis was conducted using commercial Swagelok union cells. Iron (III) diethylene triaminepentaacetate (Fe-DTPA) was pyrolized at 600, 700, 800 and 900°C at a heating rate of 10 °C min^{-1} under autogenic pressure, resulting in Fe^0/Fe_xO_y filled carbon. The as-synthesised catalysts were stirred in concentrated HCl to remove the Fe^0/Fe_xO_y core, then the HNCSs were collected by centrifuge, washed copiously with water, then ethanol and dried in a vacuum oven at 60°C overnight. The HNCSs were synthesised with different temperature from 600, 700, 800 and 900°C, followed by acid treatment, and the products were identified as HNCS61, HNCS71, HNCS81, and HNCS91, respectively.

Physical and chemical characterizations

The morphology of the HNCSs catalysts was observed by field-emission scanning electron microscope (FE-SEM, Hitachi, S-4800II) at 3 kV. The catalysts microstructures were analyzed by field-emission transmission electron microscope (FE-TEM, Hitachi, HF-3300) with 300 kV. The crystal structure of HNCSs was evaluated by X-ray diffraction (XRD, Panalytical-Empyrean) with Cu Kα radiation at a generator voltage of 40 kV and a tube current of 30 mA. Raman spectra measurements were obtained using a Thermo Nicolet ALMEGA XR, Thermo Scientific at 514 nm excitation lasers. X-ray photoelectron spectroscope (XPS, Thermo Fisher Scientific, ESCALAB250 XPS system, Theta Probe XPS system) was used with a monochromated Al K-alpha source at 15 kV and 150 W. The *ex-situ* Fe (7112 eV) K-edge X-ray absorption spectra with Ge (220) double crystal monochromator were performed at beam line BL5.2 (SUT-Nanotech-SLRI) of the Synchrotron Light Research Institute (SLRI). The XAS data for the uniformly dispersed powder samples were recorded with a proper thickness in fluorescence mode with Ar gas-filled ionization chambers as detectors. The experimental spectra to normalized XANES and Fourier transformed from k-space using k^2-weighting factor using the Athena module of the FEFFIT program.

Electrochemical characterizations

The ORR activity was studied using a rotating disk electrode (RDE) and rotating ring-disk electrode (RRDE) with a Biologic-VSP in a standard three-electrode setup with saturated calomel electrode (SCE). All potentials were calibrated and converted to RHE by adding 0.991V.[13,14] The catalyst inks were prepared by dispersing 5 mg of the catalyst in 20 µl of Nafion 5 wt% dispersion solution (Aldrich), 500 µl of isopropyl alcohol (Aldrich) and 250 µl of deionized water, and then inks were ultrasonicated for a total of 30 min. The catalyst inks were loaded with 0.5 mg cm^{-2} and 0.4 mg cm^{-2} for the RDE and RRDE experiments, respectively. All RDE and RRDE experiments were performed at room temperature in O_2-saturated 0.1M KOH electrolyte at a scan rate of 10mV s^{-1}. The slopes of ORR for RDE, based on Koutecky-Levich plots, were determined by the following equation.

$$\frac{1}{J} = \frac{1}{J_L} + \frac{1}{J_K} = \frac{1}{B\omega^{\frac{1}{2}}} + \frac{1}{J_K}$$

$$B = 0.62\, n\, F\, C_0\, D_0^{\frac{2}{3}}\, v^{-\frac{1}{6}}$$

Where, J is the experimentally measured current, J_L is the diffusion-limiting current, J_K is the kinetic current, ω is the angular velocity, F is the Faraday constant, C_0 is the saturated concentration of O_2 in 0.1M KOH (1.2 x 10^{-6} mol cm^{-3}), D_0 is the diffusion coefficient of O_2 in 0.1M KOH (1.9 x 10^{-5} cm^2 s^{-1}), and v is the kinematic viscosity of the electrolyte. "n" can calculate from slop by under plot of J^{-1} vs $\omega^{-1/2}$ and J_k is calculated from inverse of intercept.

The formation of HO_2^- and the electron transfer number was determined from RRDE using the equation:

$$OH_2^- (\%) = 200 \times \frac{I_R/N}{I_D + (I_R/N)}$$

$$n = 4 \times \frac{I_D}{I_D + (I_R/N)}$$

Where, I_D is the disk current, I_R is the ring current, and N is the ring correction coefficient in RRDE experiment was determine to be 0.37 from the reduction of $Fe(CN)_6^{4-/3-}$ redox couple. The ring potential was keep at 1.3 vs. RHE.

Fuel cell measurement

Measurements of catalytic activity were conducted in an alkaline fuel cell (AEMFC). The alkaline membrane (Tokuyama, A201) was treated by soaking in 1M KOH for 24h, and then washed copiously with DI-Water till the pH became neutral. The catalyst ink was prepared by dispersing the catalyst powder with DI-water, and AS-4 ionomer, isopropyl alcohol, and then ultrasonicating for 30 min. The catalyst was brushed onto gas-diffusion layer papers. The anode catalyst loading was 0.5 mg cm^{-2}. The non-precious catalyst loading was 4 mg cm^{-2} for the cathode catalyst. For comparison, a reference 40 wt% Pt/C cathode catalyst was prepared in a manner similar to the anode. Single cell membrane electrode assemblies (MEA) were obtained by compressing the membrane between the cathode and anode, and then hot-compressing at 80°C for 2 min with 15 kg cm^{-2}. Fuel cell performance was carried out at 60˚C, and passing rates for H_2 and O_2 were 0.4L min^{-1} using fully

humidified gases. Before taking the I-V plots, the MEAs were left at open-circuit voltage condition for 5 h, til the system reached the steady state point. All the experiments were conducted using single cells under atmospheric pressure, and no back pressure.

Results and discussion

The HNCS catalysts morphology as a function of carbonization temperature was studied by field-emission scanning electron microscope (FE-SEM) and transmission electron microscopy (TEM). Fig.1 shows the SEM and TEM images of HNCS61, HNCS71, HNCS81, and HNCS91. It is clear that after acid treatment the HNCSs show a hollow carbon sphere structure as well. The diameters observed from the TEM images are about 850±40 nm with a wall thickness of about 92±10nm. It should be noted that the pyrolysis temperature has not shown any remarkable effect on the morphology of the four prepared samples.

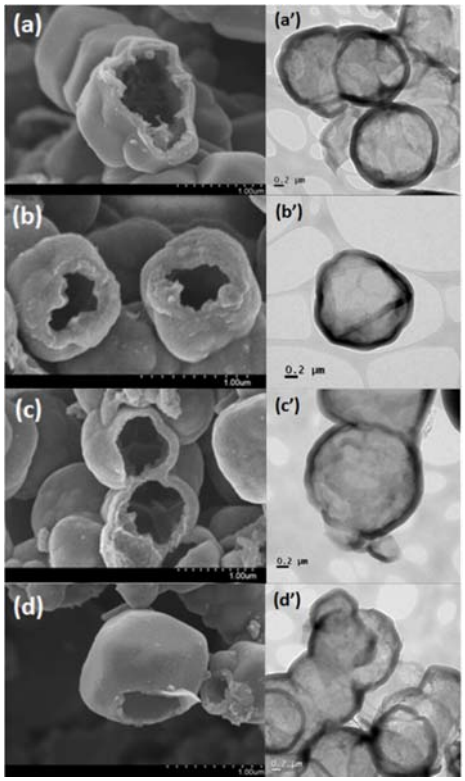

Figure 1. SEM and TEM images of (a, a') HNCS61, (b, b') HNCS71, (c, c') HNCS81, and (d, d') HNCS91, respectively.

The X-ray diffraction (XRD) patterns shown in Fig.2a are Fe-DTPA pyrolyzed product obtained at various temperatures from 600 to 900˚C. The Fe-DTPA pyrolyzed at 600˚C and 700˚C, showed peaks (2Θ) at 18.2, 30.0, 35.38, 37.0, 42.9, 53.3, 56.8, and 62.4, which are attributed to the formation of Fe_3O_4 (JCPDS no.98-008-2440), and the intensity of these peaks was reduced when the pyrolysis temperature was increased above 700˚C. When the pyrolysis temperature increased to 800˚C, three more peaks at 36.5, 42.1, and 60.5 formed, which can be assigned to FeO (JCPDS no.01-089-2468), primarily causes for loss of oxygen, indicating the existence of Fe_3O_4 and FeO phases in the Fe-DTPA@800˚C sample. It is interesting to note that the Fe_3O_4 and FeO peaks were disappeared for the Fe-DTPA@900˚C and new peaks were observed at 44.6 and 65.1, assigned to (110) and (200) planes of metallic-Fe (JCPDS no.03-065-4899), indicating that a single phase was formed during the heat-treatment at the highest temperature, 900˚C. The XRD results suggest that the structure of as-synthesised Fe-DTPA pyrolyzed product phase was different as the pyrolysis temperature was changed.

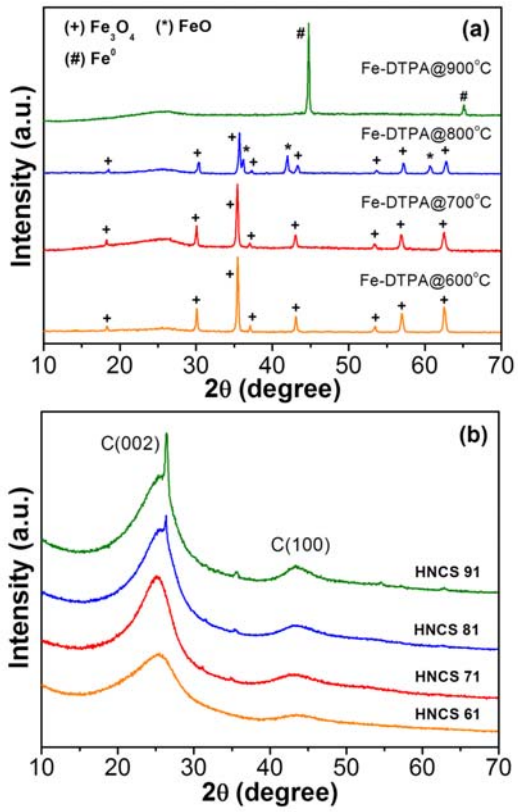

Figure 2. XRD patterns of (a) Fe-DTPA pyrolyzed products obtained at different temperatures and (b) HNCSs were prepared by acid leaching of Fe-DTPA products.

Fig.2b shows the XRD patterns of the products obtained after the acid treatment to remove Fe^0/Fe_xO_y cores from the catalyst. The XRD patterns of all HNCSs reveal the characteristic peaks of C(002) and C(100) planes of a typical turbostratic carbon structure.[15] The C(100) plane corresponds to the honeycomb structure, which is formed by sp^2 hybridized carbons, and the intensity increases as the carbonization temperature increases. On the other hand, the C(002) peak corresponding to graphene-like sheets become strong and sharper indicating the highly ordered carbon of the HNCSs samples as the temperature was increased from 600 to 900˚C. The C(002) plane of HNCS61, HNCS71, HNCS81, and HNCS91 samples were found to be at 25.34, 25.06, 26.33, and 26.37, respectively. The shift of the C(002) peak towards the lower angle suggests an increase in

planar spacing related to the doping of heteroatoms, and may indicate further Fe atom doping as well. XRD patterns of the HNCSs show that most of the Fe^0/Fe_xO_y cores were removed from the products. However, the STEM image with electron energy loss spectroscopy (EELS) spectrum acquired on the carbon shell (marked with red square in Fig.3a) clearly indicates the presence of iron and nitrogen elements in the hollow carbon surface (Fig. S1, ESI†)

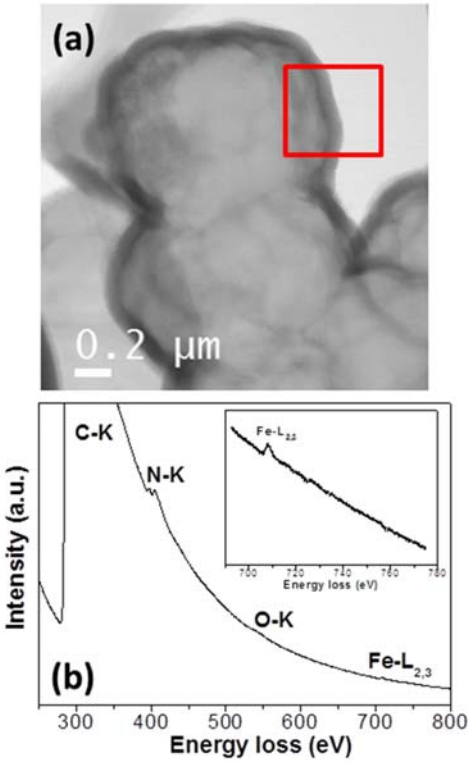

Figure 3. (a) STEM image and (b) EELS spectrum (red square indicated in STEM images) of HNCS71

Raman spectroscopy was used to investigate the nature of the carbon properties of the HNCSs (Fig.4). The Raman spectra of the HNCSs samples display two peaks, at 1360 and 1590 cm^{-1}, which are assigned to the D band and G band of carbon, respectively. The D band at 1360 cm^{-1} is related to structural disorders and defects (sp^3) of carbon, while the G band at 1590 cm^{-1} represents the ordered graphitic carbon sheet (sp^2).[16] The position of these bands are similar for all HNCSs catalysts, suggesting that the structure of all the carbons are similar, showing turbostratic features, as observed in the XRD spectra in Fig.2b. The Raman spectroscopy results indicate that the peak intensity of the G band increased with the rising carbonization temperature. The ratio of the I_D to I_G peak provides an identification of the overall carbon association, and is defined as the I_D/I_G ratio. The ratios of I_D/I_G for HNCS61, HNCS71, HNCS81, and HNCS91 were found to be 1.042, 0.94, 0.88, and 0.35, respectively. These values suggest that the HNCS91 sample exhibits more ordered graphitic carbon while HNCS61 was the most disordered graphitic carbon. This indicates that the lowest pyrolysis temperature during the synthesis resulted in the lowest degree of graphitization, corresponding with the XRD results.

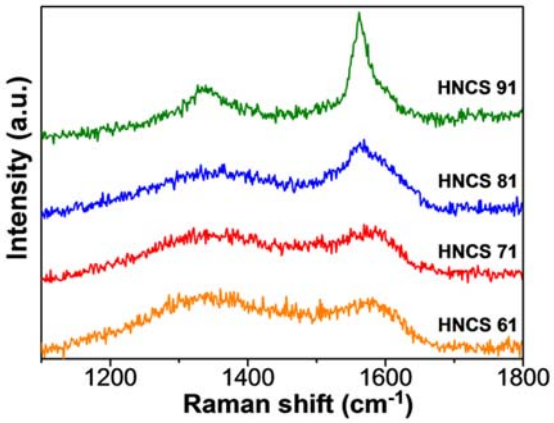

Figure 4. Raman spectra of HNCSs.

The elemental quantification of HNCSs by X-ray photoelectron spectroscopy (XPS) can provide evidence of nitrogen in the carbon framework, as shown in Fig.5. The total nitrogen content of HNCS61, HNCS71, HNCS81 and HNCS91 samples were found to be 12.5, 10.8, 6.9 and 4.1 at%, respectively, and the nitrogen content decreased with increasing temperatures from 600˚C to 900˚C. The N1s high resolution spectra was analyzed and deconvoluted into different types of nitrogen with different binding energy (BE) values: there were pyridinic-type[17,18] (~398.1), benzenoid amine-type[19] (399.6), pyrrolic-type[20] (~400.4), and graphitic and oxidized-type[11,21] (402.2) of nitrogen compounds, respectively. The content and relative ratios of different types of nitrogen changed with the heat-treatment temperature, as shown in Table S1, ESI†. Note that pyridinic, pyrrolic and graphitic nitrogen are reported to be ORR active sites. We chose to use N1 (pyridinic nitrogen), which plays an important role in evaluating the function of non-precious catalysts. The pyridinic-nitrogen has an extra electron lone pair coordinated with metal, which can localize an electron, leading to enhancements of ORR in non-precious catalysts.[7,18,22] In addition, we also considered the peak position of N1. The HNCS71 catalyst showed the pyridinic peak at 398.5 eV, which was the highest binding energy, compared with HNCS61 (398.2 eV), HNCS81 (398.1 eV), and HNCS91 (398.1 eV). The peak at this pyridinic type binding energy may also include metal coordinated nitrogen (Fe-N), as predicted by the density functional theory (DFT), with the shift of binding energy of metal-nitrogen, as compared to the pyridinic-alone, resulting in an increase in the binding energy.[23] However, this peak shift in pyridinic environment is very close, only about +0.2-0.3 eV, so it's quite difficult to differentiate for this binding energy region. From this observation, the pyridinic nitrogen peak position can be an important point to use for probing ORR active sites in metal-nitrogen catalysts. This observation is consistent with the data observed from the RDE and RRDE experimental results, which will be discussed in later sections. Further, the quantitative analyses of HNCSs samples revealed the ratio of

total N to C content (N/C ratio) of HNCS61, HNCS71, HNCS81 and HNCS91 was 0.16%, 0.13%, 0.08% and 0.04%, respectively. The N/C ratio observed in XPS also agreed well with the results observed by element analysis (Table S1 & S2, ESI†).

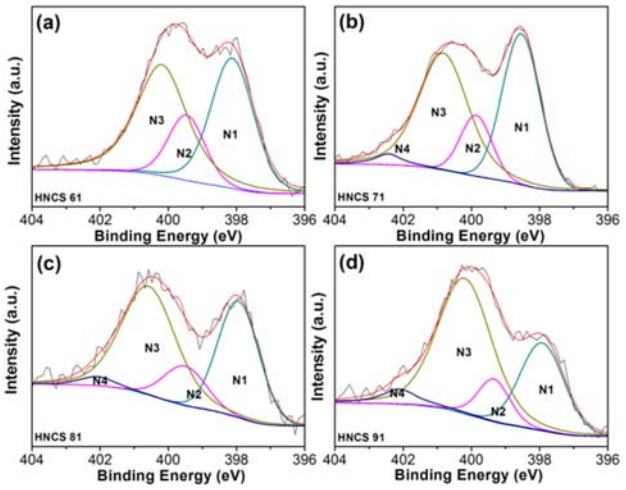

Figure 5. Deconvoluted N1s spectra of (a) HNCS61, (b) HNCS71, (c) HNCS81, and (d) HNCS91.

The effect of carbonization temperature on the electrocatalytic oxygen reduction of HNCSs was first analyzed by rotating disc electrode (RDE) experiments. A set of ORR polarization curves for HNCS71 were recorded from 800 to 2500 rpm in 0.1M KOH solution at a scan rate 10 mV s^{-1}, resulting in the current-potential curves given in Fig.6a. The ORR of HNCS71 is almost independent from the rotation speed for potentials above 0.85 V, indicating these ranges (low overpotential) are purely electrochemical kinetic. The current density at potentials lower than 0.85 V are affected by both the rotating speed and O_2 diffusion as well, and showed a good diffusion-limited current, suggesting better oxygen reduction activity, which can employed to evaluate the electron transfer number (n) during the ORR by using Koutecky-Levich (K-L) plots, as shown in the inset, Fig.6a. These plots for HNCS71 showed good parallelism and linearity for all of the potential ranges between 0.3-0.7V, indicating the n value for the ORR process was the same even at the high potentials.[24] The number of electron transfers (n) during ORR values in HNCS61, HNCS71, HNCS81 and HNCS91 evaluated at 0.5 V vs. RHE were found to be 2.41, 3.90, 3.61 and 2.96, respectively (Fig. 6a and Fig. S5, ESI†), suggesting that the HNCS71 electrocatalyst exhibits a dominant 4-electron oxygen reduction process. According to these results, HNCS71 exhibits the highest ORR activity compared with the other HNCSs, which can be attributed to the higher content of active sites. The results of all HNCSs were further compared with a Pt/C catalyst as shown in Fig. 6b. The ORR activity of Fe-DTPA complex shows negligible reduction current, indicating its poor catalytic activity towards the ORR, due to the non-conductive nature.[25] The oxygen reduction onset potentials of HNCS61, HNCS71, HNCS81, HNCS91 and Pt/C catalysts were found to be 0.79, 0.97, 0.92, 0.88 and 1.02 V, and the half-wave ($E_{1/2}$) potentials were found to be 0.61, 0.82, 0.75, 0.69 and 0.84 respectively. The $E_{1/2}$ of the HNCS71 catalyst is 20 mV lower than a Pt/C catalyst and 210 mV higher than the HNCS61 catalyst. The optimum heat-treatment temperature of HNCSs, resulting in the highest activity in $E_{1/2}$ and onset, was HNCS71.

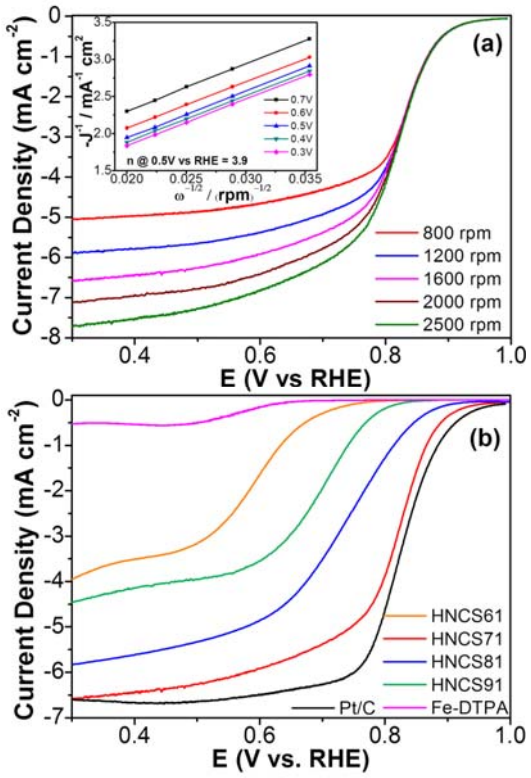

Figure 6. ORR Polarization curves of (a) HNCS71 at different rotations speed, inset; Koutecky-Levich plots of HNCS71 catalyst at different potentials. (b) Linear sweep voltammograms (LSV) curves of HNCS61, HNCS71, HNCS81, HNCS91, Fe-DTPA and Pt/C obtained from rotating disk electrode measurement in O_2-saturated 0.1M KOH at a sweep rate 10mVs^{-1}, 1600 rpm.

Temperature has been recognized as an important factor for improving the ORR activity of non-precious based catalysts. The main function of heat-treatment is to create ORR active sites. In the literature, the Zelenay group[26] synthesized an ORR catalyst by using Fe-acetate as a metal precursor, and cyanamide as a nitrogen source, and found that the activity approached that of Pt/C commercial catalyst, with superior stability. They believed that the good ORR activity could be attributed to the high density of active sites on the catalyst, which came from the many cations of metal coordinated with pyridinic-nitrogen on graphitic carbon layers at suitable pyrolysis temperature. This suggestion was also supported by results reported by Wu *et al*[27] and Byon *et al*[28]. In addition, from XPS results, heat-treatment can also produce N coordinated with C (N-C), by decomposing the N contained in the precursor, and has also shown improved ORR activity as well. Specifically, the HNCS71 catalyst exhibited higher pyridinic-type nitrogen, which can enhance the ORR activity. Further, in the case of HNCS81 and HNCS91, the active sites from both Fe-N_x and N-C might decrease as the heat-treatment temperature increases because the nitrogen content was decreased. The HNCS71 performance was also comparable

to an advanced ORR electrocatalyst that was recently reported in the literature.[20,29]

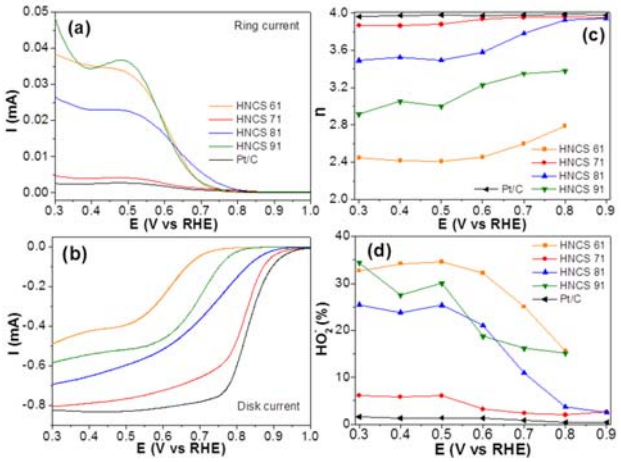

Figure 7. (a) Ring currents and (b) Disk currents of all HNCSs obtained from rotating-ring disk electrode measurement in O_2-saturated 0.1M KOH at a sweep rate 10mV s^{-1}, 1600 rpm compared with Pt/C. (c) The electron transfer number and (d) percentage of peroxide of these catalyst at various potentials obtained from RRDE experiments.

In order to further confirm the ORR activity and the selectivity of the HNCSs catalyst, we performed rotating-ring disk electrode (RRDE) measurements to evaluate the formation of peroxide species (HO_2^-) as well as the electron transfer number (n) during the ORR process. The ring and disk currents recorded at 1600 rpm in 0.1M KOH with O_2-saturated for HNCSs were compared with Pt/C commercial catalysts, and are shown in Fig.7 (a-b). It should be mentioned that the ring currents of HNCS71 from the experiment were the lowest ones, suggesting the production of HO_2^- was lowest and comparable with commercial Pt/C catalyst. As shown in Fig.7 (c-d), the ORR activities of the HNCSs catalysts show different numbers of electron transferred (n) and percentage of HO_2^- formation with carbonization temperatures from 600˚C to 900˚C. In particular, the HNCS71 catalyst exhibited a percentage of HO_2^- formation below 7%, and the n value was almost 3.9, over a potential range of 0.3-0.9 V vs RHE, indicating the oxygen reduction follows a 4-electron transfer process similar to the state-of-art Pt/C electrode. Meanwhile, with HNCS81 one can see that the value of n is close to 3.9 above 0.8 V, but at more negative potentials the n value gradually decreases and approaches almost 3.6. Furthermore, the HNCS61 and HNCS91 catalysts showed percentages of HO_2^- of about 25-35% and the value of n for oxygen reduction varied from 2.4-2.8 and 2.9-3.4 and over the potential range of 0.3-0.8V vs. RHE, which suggests poor ORR selectivity. This indicates that a mixed 2 and 4-electron process is taking place, and the reduction of O_2 produces both OH^- and HO_2^-.[30,31] The HNCS61 and HNCS91 catalysts showed poor ORR performance compared to HNCS71, which may due to insufficient carbonization temperature and a resulting low ionic conductivity for HNCS61 and weak nitrogen heteroatom content for HNCS91. It clearly illustrates that the HNCS71 catalyst can efficiently reduce oxygen via a 4-electron reduction pathway in alkaline medium. The ORR performance of the HNCSs electrocatalyst can be attributed to surface properties along with suitable amounts of nitrogen content, and proper pyrolysis temperature conditions, which significantly enhance ORR activity. However, HNCS61 has the highest nitrogen content, and also a d-spacing value higher than those of HNCS81 and HNCS91, but shows the overall lowest ORR performance of the HNCSs. In an evaluation of all the materials, HNCS71 was found to be the best ORR electrocatalyst. Based on these observations, the major parameter can be addressed from the function of pyrolysis temperature, planar-spacing and level of nitrogen doping that may include metal content, which plays the important role in ORR activity and thus likely to surpass the HNCS71 in terms of best ORR performance.

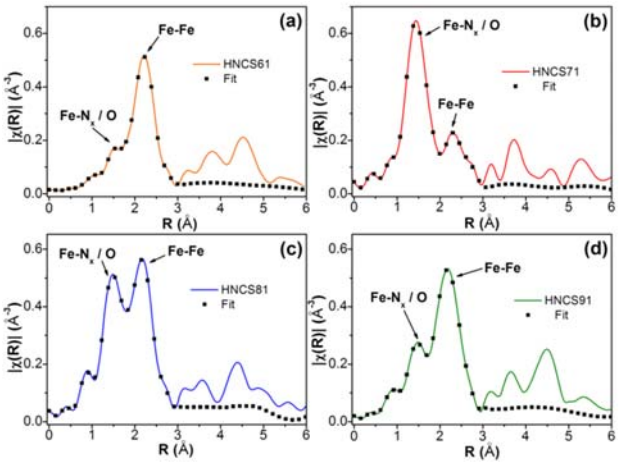

Figure 8. Fe K-edge of the k^2-weight Fourier transforms EXAFS spectra of (a) HNCS61, (b) HNCS71, (c) HNCS81, (d) HNCS91. Raw data are fitted (solid black line) for Fe-N and Fe-Fe scattering.

In order to determine the local geometric and electronic structure of the electrocatalyst, the local structure of the HNCSs catalysts were studied using X-ray absorption spectroscopy (XAS). X-ray absorption near edge structure (XANES) analysis revealed the local structure of the crystal and the oxidation state of the ion in the crystal (Fig. S6, ESI†). The coordination number of the Fe center and the nature of the neighboring N atoms were obtained from extended XAS fine structure (EXAFS). Fig. 8 demonstrates the Fe K-edge of the k^2-weighted Fourier transform EXAFS spectra in distance (R space) for the HNCSs electrocatalysts. The EXAFS data of standard Fe foil is given in Fig. S7, ESI†. From Fig. 8, the EXAFS spectra shows peaks at 1.6 Å, and this confirms the Fe coordinated with nitrogen (Fe-N_x) on the carbon framework. The peak at 2.19 Å is well matched with the spectra of metallic iron foil, suggesting this peak is mainly from the Fe-Fe scattering. The HNCS71 shows the most prominent point of Fe-N_x peak at 1.54 Å. For HNCS91, which was prepared at 900˚C, the peak located at 1.59 Å indicated the Fe-N_x are low. This means that the Fe-N_x decompose at high pyrolysis temperature. A same trend of EXAFS result reported by Nallathambi *et al*,[32] which was no detection of Co coordinated to nitrogen (Co-N_x) after pyrolyzed at high temperature (800˚C). Moreover, the peak at 2.81 Å relates to

iron oxide (Fe_xO_y) species.[33] In the ORR process of non-precious catalysts, oxygen molecules can reduce to HO_2^- at Fe-N-C or N-C active sites and further reduce again at metal-oxide sites.[34] We believe the highly synergetic M-N_x and a small amount of metal-oxide contribute greatly to the enhanced ORR performance. The EXAFS spectra were fitted to a square planar model of Fe-N_4 and Fe-Fe scatterings by using FEFFIT. The coordination number of Fe to N was found to be 1.4±0.6, 3.6±0.5, 2.7±0.3 and 2.3±0.6 for HNCS61, HNCS71, HNCS81 and HNCS91, respectively, suggesting that the HNCS71 electrocatalyst exhibits Fe-N_4 sites, which are responsible for the improved ORR process catalytic activity.[14,28,32,33]

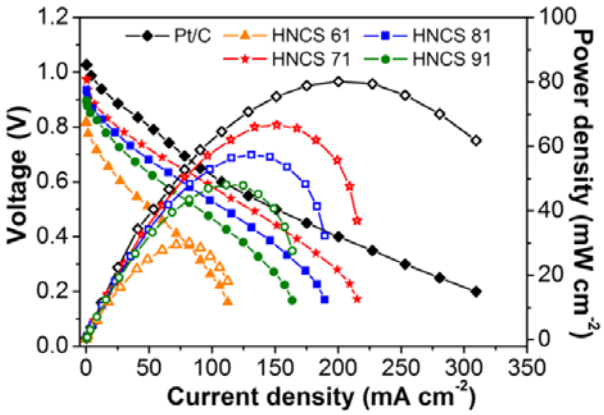

Figure 9. Polarization and power density curves of alkaline exchange membrane fuel cell performance with HNCS71 catalyst (with a loading of 4mg cm^{-2}) and Pt/C (40%Pt/C, 0.5mg cm^{-2}) at 60˚C. For MEAs, A201 membrane and AS-4 ionomer were used.

The ORR experimental results from the half-cell test motivated us to further explore applications for the HNCS electrocatalyst. Fig.9 shows the alkaline exchange membrane fuel cell (AEMFCs) performance of the HNCSs electrocatalyst (catalyst loading 4 mg cm^{-2}) and a Pt/C (40% Pt/C, catalyst loading 0.5mg cm^{-2}) cathode catalyst based membrane electrode assembly (MEA), using a fully humidified H_2-O_2 gases system at 60˚C in a single cell test. As shown in Fig.9, the open circuit voltage (OCV) of HNCS71 was 0.96V with a maximum power density (P-max) of 68 mW cm^{-2}, showing that the HNCSs can be successfully employed as a cathode catalyst in an AEMFC, while the reference Pt/C performed OCV at 1.05V with a P-max of about 80 mW cm^{-2}. The HNCS71 based MEA showed lower P-max and OCV, of about 12 mW cm^{-2} and 0.09V, respectively, compared with Pt/C. Further, the HNCS71 displayed behaviour like Pt/C in the current density region around 0-150 mA cm^{-2}. But higher than 150 mA cm^{-2}, the HNCS71 showed concentration losses, which can only be explained by poor mass-transport properties of the catalyst structure. It should be pointed out that the fuel cell data of Pt/C is in good agreement with the literature reports,[35–37] and the AEMFC performance of the HNCS71 as a cathode catalyst exhibited higher current density when compared with nitrogen doped carbon nanotubes (N-CNT),[37] and nitrogen doped nanoporous graphene (NpGr-72).[38] There are further areas that can be explored for improving AEMFC performance. Using different membranes may also improve the performance, as new membranes are under development with the goal of achieving higher OH^- transport, leading to enhanced performance.[39] Further studies are also underway to modify fuel cell operating conditions (temperature, humidity, back pressurization, flow rate of gas), MEA fabrication procedures and MEA fabrication techniques.

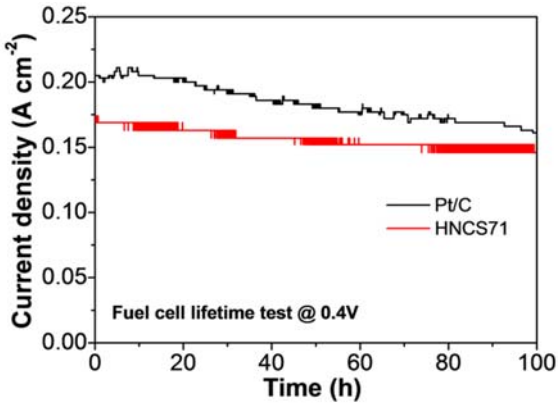

Figure 10. Alkaline membrane fuel cell durability test at a constant voltage of 0.4V in H_2-O_2 with HNCS71 and Pt/C as cathode based catalyst at 60˚C.

Fuel cell 100-hour durability tests were carried out at constant voltage 0.4V, 60°C under 100% RH and compared with Pt/C catalyst. Fig.10 shows the durability of HNCS71 and the Pt/C based cathode catalyst. After 100h, ~14% decay was observed for HNCS71 while Pt/C shows a loss of ~20%. The durability tests suggest that the decay was more prominent for Pt/C than HNCS71. The degradation behaviour of Pt/C can be explained by Pt agglomeration, Pt dissolution and might also include carbon corrosion at high potential, which can lead to the degradation,[40,41] while the degradation of HNCS71 only results from the degradation of the carbon. These results are in good agreement with the observations of Chang *et al*[24] *and* Wu *et al.*[27] They also clearly show the good catalytic durability of HNCS71 compared with the Pt/C catalyst. Durability is also an important factor must be able to test for more several hundreds of hours within a fuel cell on these catalysts reached requirements for usable applications.

Conclusions

In this work, novel non-precious catalysts comprised of hollow carbon sphere structures were successful synthesized by pyrolysis using a single precursor approach. The HNCSs were prepared at different temperatures of 600, 700, 800, and 900˚C to optimize their ORR activities. XRD results revealed that sample HNCS71 showed a shift of 2Θ, which indicated an increase of inter layer distance that comes from iron/nitrogen doping of the carbon layer. The results were in good agreement with XPS data, pointing to a pyridinic environment, and showing a shift of binding energy from the nitrogen bond to the metal, resulting in a direct 4-electron pathway in an alkaline medium. EXAFS fitting clearly showed Fe species incorporated to N,

resulting in Fe-N_4 for the HNCS71 electrocatalyst. The HNCS71 catalyst also showed proficient alkaline membrane fuel cell performance, comparable with Pt/C, as well as 100-h durability in a single cell test system. Our results indicate that Fe-DTPA is a promising precursor for metal incorporated nitrogen doped carbon catalysts, and as a new class of low-cost non-precious catalysts for high activity ORR in alkaline fuel cell applications.

Acknowledgements

The authors would like to acknowledge DGIST R&D Program of the Ministry of Education, Science and Technology of Korea (15-BD-01) for financially supported. Authors also would like to thank Synchrotron Light Research Institute (SLRI), Nakhon Ratchasima, Thailand, allowing us for the XAS measurement.

Notes and references

[a]Department of Energy Systems Engineering, Daegu Gyeongbuk Institute of Science and Technology (DGIST), Daegu, 711-873, Republic of Korea.
[b]Department of Chemistry, Faculty of Science, Mahidol University, Bangkok, 10400, Thailand.
[c]Korea Institute of Energy Research (KIER), New and Renewable Energy village, 1110-6, Baek-ryunri, Haseomyun, Bu-angun, Jeonlabukdo, Republic of Korea.
E-mail:sangarajus@dgist.ac.kr ; Fax: (+82) 53 785 6409.
†Electronic Supplementary Information (ESI) available: additional RDE, XPS and XAS results. See DOI: 10.1039/c000000x/

1 M. K. Debe, *Nature*, 2012, **486**, 43–51.
2 H. A. Gasteiger and N. M. Marković, *Science*, 2009, **324**, 48–49.
3 H. R. Colón-Mercado and B. N. Popov, *J. Power Sources*, 2006, **155**, 253–263.
4 G. Jo and S. Shanmugam, *Electrochem. Commun.*, 2012, **25**, 101–104.
5 R. Silva, D. Voiry, M. Chhowalla and T. Asefa, *J. Am. Chem. Soc.*, 2013, **135**, 7823–7826.
6 D.-W. Wang and D. Su, *Energy Environ. Sci.*, 2014, **7**, 576–591.
7 K. Gong, F. Du, Z. Xia, M. Durstock and L. Dai, *Science*, 2009, **323**, 760–764.
8 Z. Yang, Z. Yao, G. Li, H. Nie, Z. Liu, X. Zhou, X. Chen and S. Huang, *ACS Nano*, 2012, **6**, 205–211.
9 F. Jaouen, E. Proietti, M. Lefèvre, R. Chenitz, J.-P. Dodelet, G. Wu, H. T. Chung, C. M. Johnston and P. Zelenay, *Energy Environ. Sci.*, 2011, **4**, 114–130.
10 Z. Chen, D. Higgins, A. Yu, L. Zhang and J. Zhang, *Energy Environ. Sci.*, 2011, **4**, 3167–3192.
11 H. Peng, Z. Mo, S. Liao, H. Liang, L. Yang, F. Luo, H. Song, Y. Zhong and B. Zhang, *Sci. Rep.*, 2013, **3**, 1765.
12 M. Lefèvre, E. Proietti, F. Jaouen and J.-P. Dodelet, *Science*, 2009, **324**, 71–74.
13 J. Sanetuntikul, T. Hang and S. Shanmugam, *Chem. Commun.*, 2014, **50**, 9473–9476.
14 J. Y. Cheon, T. Kim, Y. Choi, H. Y. Jeong, M. G. Kim, Y. J. Sa, J. Kim, Z. Lee, T. Yang, K. Kwon, O. Terasaki, G. Park, R. R. Adzic and S. H. Joo, *Sci. Rep.*, 2013, **3**, 2715–2723.
15 H. Shi, J. N. Reimers and J. R. Dahn, *J. Appl. Crystallogr.*, 1993, **26**, 827–836.
16 F. Tuinstra, *J. Chem. Phys.*, 1970, **53**, 1126–1130.
17 C. V. Rao, C. R. Cabrera and Y. Ishikawa, *J. Phys. Chem. Lett.*, 2010, **1**, 2622–2627.
18 S. Shanmugam and T. Osaka, *Chem. Commun.*, 2011, **47**, 4463–4465.
19 F. G. Souza Jr., P. Richa, A. De Siervo, G. E. Oliveira, C. Pinto and C. H. M. Rodrigues, *Macromol. Mater. Eng.*, 2008, **239**, 675–683.
20 Y. Li, W. Zhou, H. Wang, L. Xie, Y. Liang, F. Wei, J.-C. Idrobo, S. J. Pennycook and H. Dai, *Nat. Nanotechnol.*, 2012, **7**, 394–400.
21 D. Choudhury, B. Das, D. D. Sarma and C. N. R. Rao, *Chem. Phys. Lett.*, 2010, **497**, 66–69.
22 A. Morozan, B. Jousselme and S. Palacin, *Energy Environ. Sci.*, 2011, **4**, 1238–1254.
23 K. Artyushkova, B. Kiefer, B. Halevi, A. Knop-Gericke, R. Schlogl and P. Atanassov, *Chem. Commun.*, 2013, **49**, 2539–2541.
24 Y. Chang, F. Hong, C. He, Q. Zhang and J. Liu, *Adv. Mater.*, 2013, **25**, 4794–4799.
25 Y. Zheng, J. Liu, J. Liang, M. Jaroniec and S. Z. Qiao, *Energy Environ. Sci.*, 2012, **5**, 6717–6731.
26 H. T. Chung, J. H. Won and P. Zelenay, *Nat. Commun.*, 2013, **4**, 1922.
27 G. Wu, K. L. More, C. M. Johnston and P. Zelenay, *Science*, 2011, **332**, 443–447.
28 H. R. Byon, J. Suntivich, E. J. Crumlin and Y. Shao-Horn, *Phys. Chem. Chem. Phys.*, 2011, **13**, 21437–21445.
29 Y. Liang, H. Wang, J. Zhou, Y. Li, J. Wang, T. Regier and H. Dai, *J. Am. Chem. Soc.*, 2012, **134**, 3517–3523.
30 N. Ramaswamy and S. Mukerjee, *Adv. Phys. Chem.*, 2012, **2012**, 1–17.
31 I. Kruusenberg, L. Matisen, Q. Shah, A. M. Kannan and K. Tammeveski, *Int. J. Hydrogen Energy*, 2012, **37**, 4406–4412.
32 V. Nallathambi, J.-W. Lee, S. P. Kumaraguru, G. Wu and B. N. Popov, *J. Power Sources*, 2008, **183**, 34–42.
33 U. Tylus, Q. Jia, K. Strickland, N. Ramaswamy, A. Serov, P. Atanassov and S. Mukerjee, *J. Phys. Chem. C*, 2014, **118**, 8999–9008.
34 Y. Tan, C. Xu, G. Chen, X. Fang and N. Zheng, *Adv. Funct. Mater.*, 2012, **22**, 4584–4591.
35 J. R. Varcoe, R. C. T. Slade, G. L. Wright and Y. Chen, *J. Phys. Chem. B*, 2006, **2**, 21041–21049.
36 H. Yanagi and K. Fukuta, *ECS Trans.*, 2008, **16**, 257–262.
37 C. V. Rao and Y. Ishikawa, *J. Phys. Chem. C*, 2012, **116**, 4340–4346.
38 T. Palaniselvam, M. O. Valappil, R. Illathvalappil and S. Kurungot, *Energy Environ. Sci.*, 2014, **7**, 1059–1067.
39 G. Merle, M. Wessling and K. Nijmeijer, *J. Memb. Sci.*, 2011, **377**, 1–35.
40 R. Borup, J. Meyers, B. Pivovar, Y. S. Kim, R. Mukundan, N. Garland, D. Myers, M. Wilson, F. Garzon, D. Wood, P. Zelenay, K. More, K. Stroh, T. Zawodzinski, J. Boncella, J. E. McGrath, M. Inaba, K. Miyatake, M. Hori, K. Ota, Z. Ogumi, S. Miyata, A. Nishikata, Z. Siroma, Y. Uchimoto, K. Yasuda, K.-I. Kimijima and N. Iwashita, *Chem. Rev.*, 2007, **107**, 3904–3951.
41 S. M. Alia, G. Zhang, D. Kisailus, D. Li, S. Gu, K. Jensen and Y. Yan, *Adv. Funct. Mater.*, 2010, **20**, 3742–3746.

TABLE OF CONTENTS

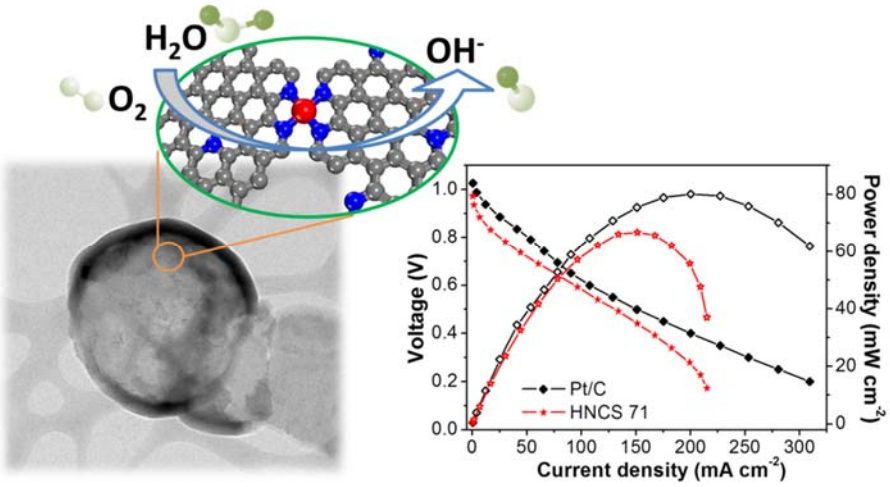

The effect of nitrogen-type, content along with metal doping in hollow carbon spheres on oxygen reduction activity is described.